J. Fluid Mech. (2003), *vol.* 477, *pp.* 215–225.
DOI: 10.1017/S0022112002002987 Printed in the United Kingdom

A large-eddy simulation study of transition and flow instability in a porous-walled chamber with mass injection

By S. V. APTE† AND V. YANG

Department of Mechanical and Nuclear Engineering, Pennsylvania State University, University Park, PA 16802, USA

(Received 13 July 2002 and in revised form 30 August 2002)

The unsteady flow evolution in a porous chamber with surface mass injection simulating propellant burning in a nozzleless solid rocket motor has been investigated by means of a large-eddy simulation (LES) technique. Of particular importance is the turbulence-transition mechanism in injection-driven compressible flows with high injection rates in a chamber closed at one end and connected to a divergent nozzle at the exit. The spatially filtered and Favre-averaged conservation equations of mass, momentum and energy are solved for resolved scales. The effect of unresolved subgrid scales is treated by using a dynamic Smagorinsky model extended to compressible flows. Three successive regimes of flow development are observed: laminar, transitional, and fully developed turbulent flow. Surface transpiration facilitates the formation of roller-like vortical structures close to the injection surface. The flow is essentially two-dimensional up to the mid-section of the chamber, with the dominant frequencies of vortex shedding governed by two-dimensional hydrodynamic instability waves. These two-dimensional structures are convected downstream and break into complex three-dimensional eddies. Transition to turbulence occurs further away from the wall than in standard channel flows without mass injection. The peak in turbulence intensity moves closer to the wall in the downstream direction until the surface injection prohibits further penetration of turbulence. The temporal and spatial evolution of the vorticity field obtained herein is significantly different from that of channel flow without transpiration.

1. Introduction

The combustion-induced flow field in a solid-propellant rocket motor can be thought of as mass injection from the burning surface. Several experimental studies have been conducted (Traineau, Hervat & Kuentzmann 1986; Dunlap *et al.* (1990, 1992) to characterize motor internal flow evolution by injecting inert gases through the sidewalls of porous chambers, as shown in figure 1. Although measurements of turbulence intensities and mean velocity profiles are available, detailed insight into the unsteady flow field is lacking. In realistic motor configurations, the flow accelerates from the head end, resulting in streamwise inhomogeneity, undergoes transition to turbulence in the mid-section of the motor, becomes fully turbulent further downstream, and finally reaches supersonic conditions at the exit of the nozzle.

† Present address: Bldg. 500, ME/FPC, 488 Escondido Mall, Stanford, California, CA 94305, USA; sapte@stanford.edu

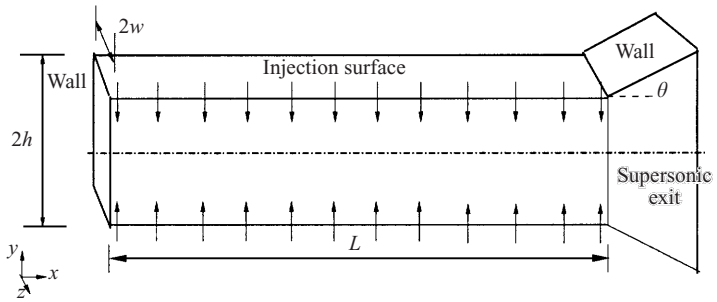

FIGURE 1. Schematic diagram of a nozzleless solid rocket motor.

The flow field is essentially incompressible and laminar in the upstream region and becomes compressible from the mid-section of the motor. The role of mass injection in suppression/enhancement of turbulence production in such a configuration has not been investigated in detail.

Our earlier numerical investigations of injection-driven flows in rocket motors (Apte & Yang 2000*a*, 2001, 2002; Apte 2000) indicated two-dimensional roll-up-like vortical structures throughout the chamber. These two-dimensional simulations captured the mean-flow properties accurately, but underpredicted the turbulence production and shear-stress levels. As the flow accelerates from the head end, pressure and density decrease towards the exit nozzle. The effect of injection on the flow development may decrease in the downstream region where the axial velocities in the core flow become significantly high. Increased Reynolds numbers based on axial velocity may set up hydrodynamic instabilities and cause three-dimensional breakdown of the roll-up structures. This in turn would lead to higher turbulence production and dissipation rates, which were not captured by the previous studies mainly because of the lack of vortex-stretching mechanism. The present work attempts to investigate the above-mentioned phenomena by performing large-eddy simulations (LES). Emphasis is placed on exploring the three-dimensional vorticity dynamics, compressibility effects, and turbulence transition in flows with high mass injection.

LES was used by Piomelli, Moin & Ferziger (1991) to study incompressible turbulent flows through channels with low transpiration rates. Sumitani & Kasagi (1995) performed direct numerical simulations (DNS) of channel flows with blowing from one wall and suction through the opposite side at low transpiration rates of $v_w/u_\tau = 0.05$, where v_w is the injection velocity and u_τ the friction velocity. Results of these studies can be summarized as follows: when fluid is injected, the boundary layer becomes thicker, the skin friction decreases, and turbulent fluctuations are enhanced. Transpiration greatly alters the wall-layer dynamics and tends to stimulate the near-wall turbulence activity so that the Reynolds stresses and turbulent heat fluxes are increased, whereas suction has the reverse influence.

Nicoud, Poinsot & Minh (1995) performed DNS at high injection rates, $v_w/u_\tau = 1.4$, in an attempt to reproduce flow conditions representative of solid rocket motors and to study the effect of high blowing rates on the wall-layer dynamics. The injection and centreline Reynolds numbers of 87 and 2985 were small compared to those of nozzleless rocket motor configurations. They observed an inflection point on the mean axial velocity profile near the wall ($y/h \sim 0.07$). Substantial reduction in wall shear stress was observed compared to channel flows without injection for the same centreline velocity. Ciucci *et al.* (1998) conducted a detailed comparison of the DNS

results with standard k–ϵ turbulence closure schemes and the $\bar{v}^2$–f model. They pointed out that the appropriate velocity scale for turbulent transport near the wall is $\bar{v}^2$ instead of the turbulence intensity and showed considerable improvement over standard k–ϵ models (Beddini 1986; Sabnis *et al.* 1989).

All of the LES and DNS studies reported above have been performed using idealized periodic domains, with numerical schemes based on either incompressible flow solvers or spectral methods. Nicoud *et al.* (1995) used a compressible flow solver, but did not report high Mach numbers in their computation. The present configuration, however, involves upstream incompressible and downstream compressible regimes and necessitates use of an all-Mach-number numerical scheme, capable of treating the numerical stiffness arising from the wide variations of flow structures (Hsieh & Yang 1997). This numerical study also serves as a foundation for our parallel efforts to explore the effects of unsteady heat release and turbulent flame dynamics on the microscale motions close to the propellant surface and macroscale motions in the bulk of the chamber (Roh, Apte & Yang 1998; Apte & Yang 2000*b*).

The main objectives of this paper are: (i) to characterize the three-dimensional flow evolution in a porous chamber with surface mass injection at high Reynolds and Mach numbers, and (ii) to identify the effects of surface injection on transition to turbulence and the mean velocity profiles.

2. Theoretical formulation

Figure 1 shows the physical model for the problem, a rectangular porous chamber with surface mass injection simulating the flow development in a nozzleless solid-propellant rocket motor studied experimentally by Traineau *et al.* (1986). The chamber is closed at the head end and is connected downstream with a choked divergent nozzle at the exit. The two sidewalls in the spanwise direction are non-transpiring. Air is injected uniformly through the porous walls at a pre-specified pressure and mass flow rate.

The spatially filtered, Favre-averaged governing equations for compressible flows (Erlebacher *et al.* 1990) are solved in the present study. The filtered forms of these equations can be written as

$$\frac{\partial \rho^r}{\partial t} + \frac{\partial (\rho^r \tilde{u}_k^r)}{\partial x_k} = 0, \tag{2.1}$$

$$\frac{\partial (\rho^r \tilde{u}_k^r)}{\partial t} + \frac{\partial (\rho^r \tilde{u}_k^r \tilde{u}_l^r)}{\partial x_l} = -\frac{\partial p^r}{\partial x_k} + \frac{\partial \sigma_{kl}^r}{\partial x_l} + \frac{\partial \tau_{u_l u_k}}{\partial x_l}, \tag{2.2}$$

$$\frac{\partial (\rho^r \tilde{e}^r)}{\partial t} + \frac{\partial (\rho^r \tilde{h}^r \tilde{u}_k^r)}{\partial x_k} = -\frac{\partial q_k^r}{\partial x_k} + \frac{\partial (u_l \tau_{kl})^r}{\partial x_k} - \frac{\partial \tau_{u_k h}}{\partial x_k} - \frac{\partial \tau_{u_k u_l u_l}}{\partial x_k}, \tag{2.3}$$

where ρ is the density, u_k the velocity components, p the thermodynamic pressure, h the specific total enthalpy, e the specific total internal energy, T the temperature, σ_{kl} the viscous stress, q_k the thermal diffusion, and ϕ the viscous dissipation (Apte & Yang 2001). The superscript 'r' denotes resolved-scale motions. The ideal-gas equation of state, $p^r = \rho^r R \tilde{T}^r$ is used. The specific total energy and enthalpy are given as

$$\tilde{e}^r = C_p \tilde{T}^r - p^r/\rho^r + \tilde{u}_k^r \tilde{u}_k^r/2$$

and

$$\tilde{h}^r = C_p \tilde{T}^r + \tilde{u}_k^r \tilde{u}_k^r/2,$$

respectively. Here, C_p is the specific heat at constant pressure and is assumed to

be constant in the present cold-flow simulation, as the temperature variation within the flow field of interest is not significant. The subgrid-scale correlations, $\tau_{u_k u_l}$, $\tau_{u_k h}$, $\tau_{u_k u_l u_l}$ and $(u_l \tau_{kl})^r$, are closed using the compressible-flow version of the dynamic Smagorinsky model (DSM) (Moin *et al.* 1991).

The method of characteristics is used to specify the boundary conditions. For the subsonic inflow through the porous surface, four conditions need to be specified for the present three-dimensional computation. The mass and energy fluxes are kept constant and the injection velocity is assumed to be vertical (i.e. $\tilde{u}^r = 0, \tilde{w}^r = 0$). The effects of surface roughness and pseudo-turbulence at the injection surface were explored by imposing broadband white noise on the mean mass flow rate. At the head end of the motor, the gradients of the axial pressure and vertical velocity are set to zero, along with the adiabatic condition. Application of a slip condition at the head end is necessary to avoid a numerically induced recirculating flow at the injection surface (Apte 2000). No-slip conditions are specified on the sidewalls. The supersonic outflow requires no boundary conditions, according to the method of characteristics. The flow variables at the exit are extrapolated from those within the computational domain.

3. Numerical scheme

Although LES has been used to study a variety of turbulent flows, the majority of these applications involve low Mach number or incompressible flow computations. LES has not been broadly applied to compressible turbulent flows, although this aspect has recently received considerable attention. For such simulations, an accurate numerical scheme is essential for resolving various time and length scales of turbulent motions. In LES, significant flow energy is present at high wavenumbers and the numerical scheme should be non-dissipative at these wavenumbers. Numerical schemes for compressible flows based on collocated mesh and central differences for spatial derivatives usually add artificial (numerical) dissipation to suppress oscillations at high wavenumbers. The present all-Mach-number, finite-volume numerical scheme employs a fourth-order Runge–Kutta scheme for temporal discretization and fourth-order central differences for spatial discretization. In order to obtain numerical stability over a broad range of Mach number, sixth-order artificial dissipation is added. Our earlier work (Apte & Yang 2001) addressed the effect of these dissipation terms on the overall accuracy of the simulations by conducting a detailed analysis of errors involved in resolving the turbulence energy spectrum after one eddy lifetime. It was shown that for moderate resolutions, the effect of subgrid-scale models is predominant, and artificial dissipation terms only serve to obtain numerical robustness and in turn stabilize the scheme.

4. Unsteady flow evolution in a porous chamber with mass injection

The analysis described above is used to study the flow development in a simulated nozzleless rocket motor, as shown schematically in figure 1. The chamber measures 48 cm in length, 2 cm in height, and 4 cm in width. The nozzle at the exit is 3.2 cm long with a divergence angle of 15°. The chamber configuration and flow parameters studied are based on the experiment of Traineau *et al.* (1986). Air is injected through the porous walls at a total temperature of 260 K and a total pressure of 3.142 atm. The mean injection mass flux is kept constant at $\bar{\dot{m}}''_w = 13\,\mathrm{kg\,m^{-2}\,s^{-1}}$, giving the injection velocity of $3.1\,\mathrm{m\,s^{-1}}$ and injection Reynolds number Re_w of 15 000 at the head end. The normalized injection rate, v_w/u_τ, varies from 1.5 to 6 in the axial direction.

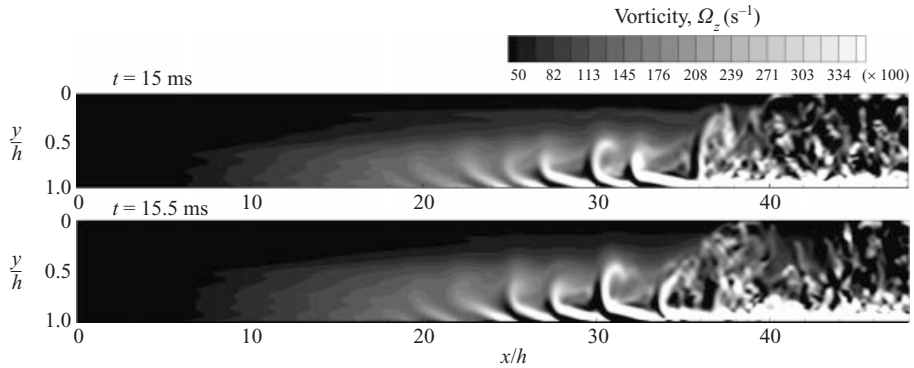

FIGURE 2. Snapshots of spanwise vorticity with spatial averaging in the z-direction.

The numerical calculation is initialized with the analytical velocity profile for an inviscid incompressible flow with surface mass injection (Taylor 1956; Culick 1966),

$$\frac{\tilde{u}^r}{\tilde{u}^r_c} = \cos\left(\frac{\pi}{2}\frac{y}{h}\right) \quad \frac{\tilde{v}^r}{\tilde{v}^r_w} = \sin\left(\frac{\pi}{2}\frac{y}{h}\right), \tag{4.1}$$

where the subscript 'c' represents the centreline. White noise is introduced in the inflow mass flux to perturb the mean flow for turbulence transition. Two magnitudes of perturbation, at 1% and 90% of the mean quantity, are considered. The high level of perturbation at the surface is employed to facilitate comparison with experimental data. These perturbations, however, are the combined effect of oscillations in the density and vertical injection velocity. The computational domain consists of $640 \times 140 \times 100$ cells in the axial, vertical, and spanwise directions, respectively. A uniform grid is used in the x-direction, while the grid is stretched toward the surfaces in the y- and z-directions with the smallest grid size on the order of 50 μm. In order to obtain turbulence characteristics, the wall-layer dynamics must be captured accurately. The wall shear stresses are smaller in injection-driven flows and the first grid point from the wall need not be located at $y^+ < 5$, as for channel flows without surface transpiration. In the present simulations, the near-wall grid resolution in terms of the wall unit changes from $y^+ \sim 2$ at $x/h = 0$ to around $y^+ \sim 12$ near the throat region ($x/h = 46$). The time step is fixed at 1×10^{-8} s for time-accurate simulations. Turbulence occurs after 4–5 ms of the physical time starting from the flow initialization based on equation (4.1). Stationary oscillations are obtained in the period 8–17 ms, and the mean flow properties are evaluated in this time zone. The computation took around 8000 CPU-processor hours on 18 processors of a Cray T3E.

4.1. *Instantaneous flowfield*

Figure 2 shows the time evolution (for half of the eddy turnover time) of spanwise vorticity in the (x, y)-plane obtained with spatial averaging in the z-direction. Only the lower half of the chamber is presented, where $y/h = 1$ corresponds to the injection surface. The flow entering vertically into the chamber turns to align smoothly with the axial axis, thus rendering a rotational flowfield (Flandro 1995). Three different regimes of flow development are clearly observed: laminar, transitional, and fully turbulent. Near the head end, turbulent fluctuations are small and the flow is mostly laminar. Transition to turbulence occurs around $x/h = 20$–25, and the flow becomes highly turbulent further downstream. Vorticity is rapidly convected away from the surface in this inertia-dominated flow, as evidenced by the presence of large energy-

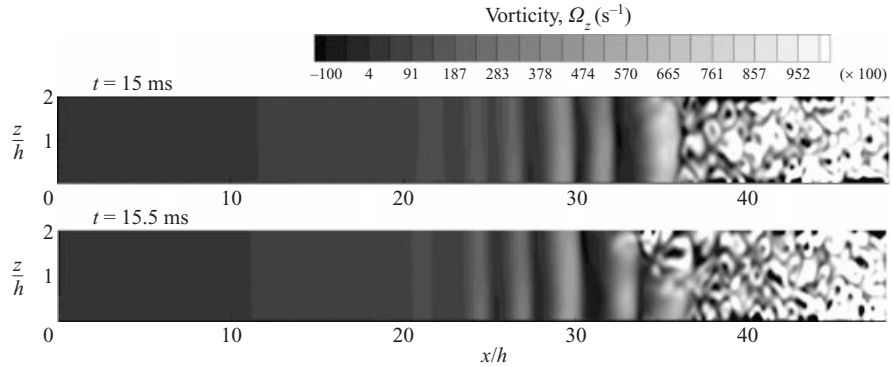

FIGURE 3. Time evolution of spanwise vorticity in the (x, z)-plane, $y/h = 0.98$.

carrying structures. The white noise introduced at the injection surface grows into a three-dimensional broadband spectrum with the hydrodynamically unstable modes displaying large-scale oscillations. Roll-up vortex structures are clearly visible. These structures are inclined in a direction opposite to the mean axial flow near the injection surface. In the present simulation, the density decreases and Mach number increases towards the exit nozzle. Accordingly, the injection velocity increases by more than 100% over the length of the chamber in order to keep the injection mass flow rate constant. A breakdown of the roll-up structures, generating smaller three-dimensional eddies, is observed beyond $x/h = 34$.

Figure 3 shows the evolution of spanwise vorticity in the (x, z)-plane at $y/h = 0.98$, where $z/h = 0$ and 2 correspond to the wall and centreline, respectively. Straight vertical streaks in vorticity indicate the coherence of the spanwise vorticity in the (y, z)-plane. The vortical structures are basically two-dimensional in the upstream region and break down to form three-dimensional structures around $x/h = 35$. It was found that these bands of vorticity oscillate back and forth over a period of around 1 ms and travel at an approximate speed of 10–15 m s^{-1}.

The transition mechanism observed herein is significantly different from channel flows without surface mass injection (Kim, Moin & Moser 1987), where the two-dimensional roll-up structures were absent. Narasimha & Sreenivasan (1979) pointed out the effect of surface mass injection on transition to turbulence. In a fully developed turbulent boundary layer without transpiration, the high-speed outer fluid moves close to the wall, and the sub-layer is thinned triggering the Taylor–Görtler instability. Surface injection, however, increases the wall-layer thickness, reduces the shear stresses, and prohibits penetration of the outer fluid close to the wall. This leads to the formation of roll-up-like structures as observed in figure 2. The effect of mass injection is to increase the inclination of the near-wall structures with respect to the wall. In the mid-section of the chamber, the axial velocity has a strong convex curvature suppressing the instability and retaining the two-dimensionality of the vortical structures. Further downstream, compressibility effects prevail, with the average Mach number approaching unity. The radial profile of axial velocity is flattened in a manner analogous to that arising from turbulence in flows without injection. The wall shear stress increases rapidly beyond this point.

Balakrishnan, Linan & Williams (1992) attribute the generation of turbulence in an injection-driven duct closed at the head end to two sources: (*a*) the instability of the boundary layer developed on the head endwall where the flow decelerates

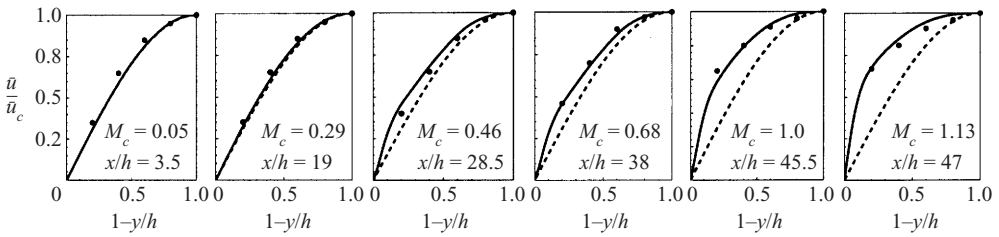

FIGURE 4. Variations of normalized mean axial velocity in the vertical direction: ——, present LES; - - -, laminar incompressible (equation (4.1)); • • •, Traineau *et al.* (1986).

in the vertical direction from the injection surface towards the centreline, and (*b*) laminar flow instabilities near the porous walls downstream. The first mechanism gives rise to head end-wall separations which grow in the downstream direction. This mechanism is absent in the present simulations as the slip condition is enforced at the head endwall. This enables us to isolate one mechanism of turbulence generation and also simplifies the computation as the boundary layer on the head endwall is not resolved. The random perturbations introduced at the injection surface, on the other hand, result in asymmetric disturbances which grow away from the porous wall in the mid-section of the chamber and produce transition to turbulence.

4.2. *Mean flow structure*

Figure 4 shows the evolution of mean axial velocity profiles. The flow is predominantly incompressible and laminar in the upstream region. Deviation from the cosine profile (4.1) is observed beyond $x/h = 20$. The DNS by Nicoud *et al.* (1995) for $Re_w \sim 87$ in a periodic domain indicates the presence of an inflection point in the axial velocity profile near the porous wall. For the same centreline velocity, the channel flow without injection gives rise to higher wall shear stresses. Varapaev & Yagodkin (1969) showed from their stability analysis that for a small injection Reynolds number, $Re_w < 300$, the transverse velocity component has a destabilizing effect and reduces the critical Reynolds number for transition. For $Re_w > 300$, however, the stabilizing effect due to the favourable pressure gradient dominates. In the present computation, $Re_w \sim 15 \times 10^3$, and the destabilizing effect of the transverse velocity component is not observed. The flow disturbances at the injection surface grow rapidly as they are transported away from the wall. Transition to turbulence occurs in the mid-section of the chamber as indicated by the flattening of the axial velocity profiles for $20 < x/h < 34$. The axial velocity along the centreline increases almost linearly from the head end till $x/h = 34$, beyond which the flow accelerates rapidly and the compressibility effect plays an important role. The axial velocity profiles there are considerably flattened, analogously to a channel flow without injection.

In order to further investigate the flow transition characteristics, we examined the axial variation of the skin friction coefficient, $C_f = 2(u_\tau/u_b)$, and the momentum flux coefficient

$$\beta = \int_0^h \bar{\rho}(\bar{u}^2)\,\mathrm{d}y/\overline{\rho_b}(\overline{u_b}^2)h,$$

where the subscript '*b*' denotes the bulk mean quantity obtained by averaging the corresponding flow property over a given cross-section of the chamber, and $u_\tau = \sqrt{\mu/\bar{\rho}(\partial\bar{u}/\partial y)}$ is the friction velocity. Figure 5(*a*) shows a monotonic decline in C_f till the mid-section of the chamber, and a sharp increase further downstream. This suggests that surface mass injection reduces wall shear stress till the mid-section of

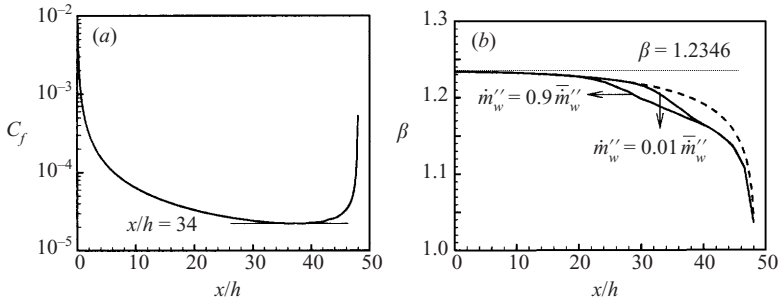

FIGURE 5. Axial variations of (a) skin friction coefficient, C_f, and (b) momentum flux coefficient, β: ——, present LES; - - -, laminar compressible computation, Apte (2000).

the motor. Further downstream, however, increased compressibility effects along with the three-dimensional breakdown of the vortical structures shown in figures 2 and 3 give rise to flattened velocity profiles and significantly increase the wall shear stresses.

Figure 5(b) shows the distribution of the momentum flux coefficient, β, which has a constant value of 1.234 for a laminar incompressible flow based on equation (4.1). The corresponding variation for laminar compressible flow (Apte 2000) is also included for comparison. The decreased density due to flow acceleration in the axial direction alters the vertical variation of the axial velocity and consequently causes a monotonic decrease in β. The effect of surface-generated turbulence on the flow evolution was also investigated. For a high level of wall turbulence (i.e. $\dot{m}''_w = 0.9\overline{\dot{m}''_w}$), the transition of the mean velocity profile occurs upstream of the motor ($x/h = 20$). The transition point shifts downstream ($x/h = 30$) with a lower level of wall turbulence (i.e. $\dot{m}''_w = 0.01\ \overline{\dot{m}''_w}$). Between $x/h = 20$ and 40, the β values are lower than those corresponding to the laminar, compressible flow solution. Further downstream, the momentum flux coefficient is considerably influenced by the compressibility effect and follows the curve for the laminar flow solution.

4.3. *Turbulence characteristics and energy spectra*

Figure 6 shows the vertical variations of turbulence intensity ($I = \sqrt{\overline{u'^2} + \overline{v'^2} + \overline{w'^2}}$) and Reynolds stress ($\overline{u'v'}$) at various axial locations. The Reynolds stress and turbulence intensity predicted well the experimental data of Traineau *et al.* (1986). As a result of the asymmetric growth of disturbances introduced at the injection surface (Balakrishnan *et al.* 1992), transition to turbulence occurs further away from the wall compared to turbulent channel flows without injection (Kim *et al.* 1987). The peak in turbulence production shifts closer to the wall, from $y/h = 0.6$ at $x/h = 20$ to $y/h = 0.83$ at $x/h = 46$, as the flow accelerates downstream. However, the increased injection velocity due to the fluid compressibility effect in the downstream region limits the penetration of turbulence close to the surface. The vertical location of the peak turbulence intensity thus remains unchanged beyond $x/h = 34$.

Figure 7 shows the power spectral density of pressure fluctuations at various axial locations with $y/h = 0.9$ and $z/h = 2$. The peak magnitude of pressure fluctuation is around 1% of the mean chamber pressure at the head end. The magnitude of pressure oscillation decreases in the axial direction and is correlated with oscillatory vorticity. Low levels of pressure correspond to concentrated vortical structures and highly rotational flows. The dominant frequency of pressure fluctuation at around 1950 Hz arises from the sweeping of large-scale structures past the spatial location under consideration.

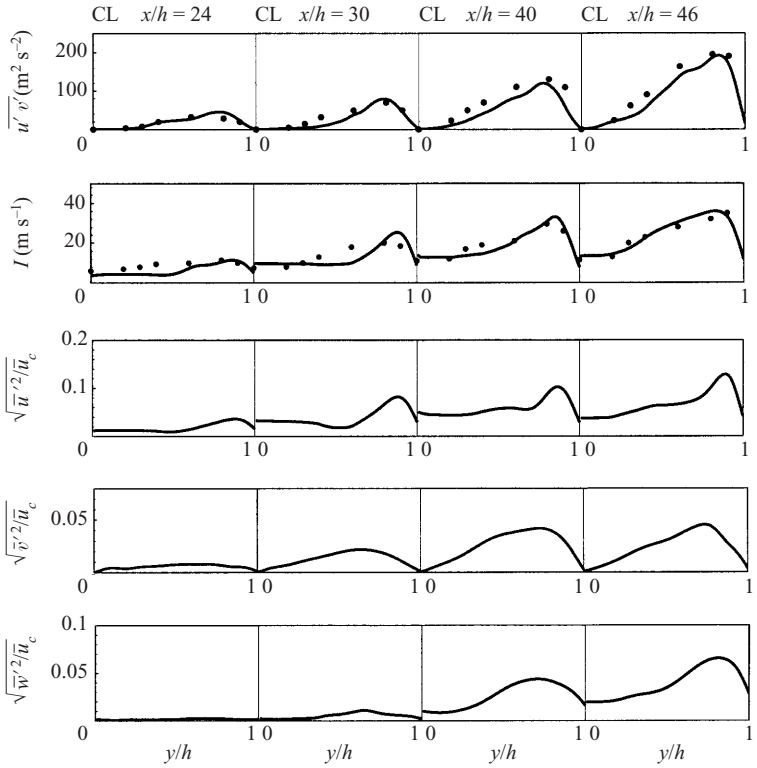

FIGURE 6. Vertical variations of turbulence intensity, Reynolds stress, and fluctuations of velocity components: ——, present LES; • • •, Traineau *et al.* (1986).

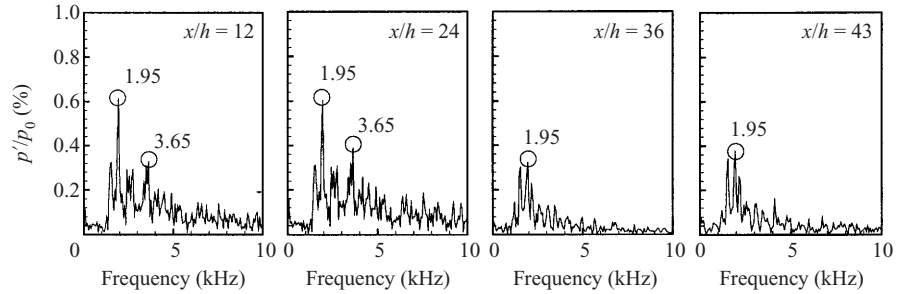

FIGURE 7. Power spectral densities of pressure fluctuations normalized by head-end pressure, p_0, at various axial locations.

Figure 8 shows the power spectral distributions of axial velocity fluctuations at various vertical locations in the transition region, $x/h = 34$ and $z/h = 2$. The magnitude of the axial velocity fluctuations decreases away from the injection surface. The decrease in the spectrum at higher frequencies also indicates minimal aliasing errors. This result ensures that the energy spectrum is captured well throughout the chamber, which further confirms the adequacy of the computational grid.

The presence of dominant frequencies close to multiples of 1950 Hz indicates a strong vortex-pairing phenomenon. Recently, Casalis, Avalon & Pineau (1998) and Ugurtas *et al.* (2000) conducted an analytical study and experimental measurements to investigate the flow instability and acoustic resonance of internal flows in rocket

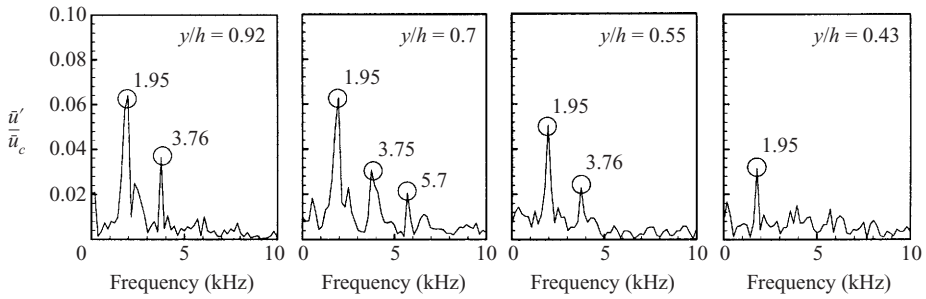

FIGURE 8. Power spectral densities of axial velocity fluctuations normalized by centreline velocity, $\bar{u}_c$, at various vertical locations, $x/h = 34$ and $z/h = 2$.

motors. Results on velocity and pressure fluctuations were characterized the Strouhal number $St = fh/v_w$. The present study indicates that $St \sim 6$, based on the frequency of 1950 Hz. Ugurtas *et al.* (2000) also predicted a similar range of the Strouhal number for different injection velocities and chamber configurations in an effort to investigate the parietal vortex shedding phenomenon in rocket motors.

5. Conclusion

A large-eddy simulation of the flow development in a porous-walled chamber with surface mass injection has been performed. The flow field is characterized by three distinct regimes: laminar, transitional, and fully developed turbulent flows. The flow is essentially two-dimensional in the upstream region, with the dominant frequencies of vortex shedding governed by two-dimensional hydrodynamic instability waves. The balance between pressure gradient and inertia force dictates the local flow evolution. Roller-like vortical structures coherent in the spanwise directions are observed, unlike the low-speed streak formation in channel flows without injection. Surface injection increases the wall-layer thickness, reduces the shear stresses, and prohibits deep penetration of outer fluid close to the wall. This leads to the formation of coherent roll-up vortices in the mid-section. Transition to turbulence occurs farther away from the wall. Further downstream, increased axial velocity overcomes the effect of mass injection, forming three-dimensional eddies. The vortex-stretching mechanism included implicitly in the present study is responsible for accurate prediction of the turbulence production and dissipation rates. High levels of surface roughness and pseudo-turbulence initiate early transition to turbulence, but their effect on the mean flow field is minimal.

This work was partly sponsored by the Pennsylvania State University and partly by California Institute of Technology's Multi University Research Initiative (MURI) program under Grant No. N00014-95-1-1338. The authors appreciate use of the parallel cluster at the Alaska Supercomputing Center.

REFERENCES

APTE, S. V. 2000 Unsteady flow evolution and combustion dynamics of homogeneous propellant in a rocket motor. PhD thesis, The Pennsylvania State University.

APTE, S. V. & YANG, V. 2000*a* Effects of acoustic oscillation on flow development in a simulated nozzleless rocket motor. *Prog. Aero. Astro.* **185**, 791–822.

Apte, S. V. & Yang, V. 2000*b* Turbulent flame dynamics of homogeneous solid propellant in a rocket motor. *Proc. Combust. Inst.* **28**, 903–910.

Apte, S. V. & Yang, V. 2001 Unsteady flow evolution in a porous chamber with surface mass injection, I: free oscillations. *AIAA J.* **39**, 1577–1586.

Apte, S. V. & Yang, V. 2002 Unsteady flow evolution in a porous chamber with surface mass injection, II: acoustic excitations. *AIAA J.* **40**, 244–253.

Balakrishnan, G., Linan, A. & Williams, F. A. 1992 Rotational inviscid flow in laterally burning solid-propellant rocket motors. *J. Propul. Power* **8**, 1167–1176.

Beddini, R. A. 1986 Injection induced flows in porous-walled ducts. *AIAA J.* **24**, 1766–1773.

Casalis, G., Avalon, G. & Pineau, J.-P. 1998 Spatial instability of planar channel flow with fluid injection through porous walls. *Phys. Fluids* **10**, 2558–2568.

Ciucci, A., Iaccarino, G., Moser, R., Najjar, F. & Durbin, P. 1998 Simulation of rocket motor internal flows with turbulent mass injection. *Proc. Summer Prog. Center for Turbulence Research, Stanford University*, pp. 245–266.

Culick, F. E. C. 1966 Rotational axisymmetric mean flow and damping of acoustic waves in solid propellant rocket motors. *AIAA J.* **4**, 1462–1464.

Dunlap, R., Blackner, A. M., Waugh, R. C., Brown, R. S. & Willoughby, P. G. 1990 Internal flow field studies in a simulated cylindrical port rocket chamber. *J. Propul. Power.* **8**, 1167–1176.

Dunlap, R., Blackner, A. M., Waugh, R. C., Brown, R. S. & Willoughby, P. G. 1992 Internal flow field studies in a simulated cylindrical port rocket chamber. *J. Propul. Power.* **6**, 690–704.

Erlebacher, G., Hussaini, M. Y., Speziale, C. G. & Zang, T. A 1990 Toward the large-eddy simulation of compressible turbulent flows. *ICASE Paper* 87-20.

Flandro, G. A. 1995 Effects of vorticity on rocket combustion stability. *J. Propul. Power.* **11**, 607–625.

Hsieh, S.-H. & Yang, V. 1997 A preconditioned flux-differencing scheme for chemically reacting flows at all Mach numbers. *Intl J. Comput. Fluid Dyn.* **8**, 690–705.

Kim, J., Moin, P. & Moser, R 1987 Direct numerical simulation of fully developed channel flow. *J. Fluid Mech.* **177**, 136–166.

Narasimha, R. & Sreenivasan, K. R. 1979 Relaminarization of fluid flows. *Adv. Appl. Mech.* **19**, 221–309.

Moin, P., Squires, K., Cabot, W. & Lee, S. 1991 A dynamic subgrid-scale model for compressible turbulence and scalar transport. *Phys. Fluids* **3**, 2746.

Nicoud, F., Poinsot, T. J. & Minh, H. H. 1995 Direct numerical simulation of a turbulent flow with massive uniform injection. *10th Symp. Turbulent Shear Flows*, vol. 3, pp. 13–18. Pennsylvania State University, USA.

Piomelli, U., Moin, P. & Ferziger, J. 1991 Large eddy simulation of flow in a transpired channel. *J. Thermophys.* **5**, 124–128.

Roh, T. S., Apte, S. V. & Yang, V. 1998 Transient combustion response of homogeneous solid propellant to acoustic oscillations in a rocket motor. *Proc. Combust. Inst.* **27**, 2335–2341.

Sabnis, J. S., Madabhushi, R. K., Gibeling, H. J. & McDonald, H. 1989 On the use of k–ϵ turbulence model for computation of solid rocket internal flows *AIAA Paper* 89-2558.

Sumitani, Y. & Kasagi, N. 1995 Direct numerical simulation of turbulent transport with uniform wall injection and suction. *AIAA J.* **33**, 1220–1228.

Taylor, G. I. 1956 Fluid flow in regions bounded by porous surfaces. *Proc. R. Soc. Lond.* **234**, 456–475.

Traineau, J. C., Hervat, P. & Kuentzmann, P. 1986 Cold-flow simulation of a two-dimensional nozzleless solid-rocket motor. *AIAA Paper* 86-1447.

Ugurtas, B., Avalon, G., Lupoglazoff, N., Vuillot, F. & Casalis, G. 2000 Stability and acoustic resonance of internal flows generated by side injection. *Prog. Aero. & Astro.* **185**, 823–836.

Varapaev, V. N. & Yagodkin, V. I. 1969 Flow stability in a channel with porous walls. *Izv. Akad. Nauk SSSR, Mekh. Zhid. i Gaza* **4**, 91–95.